

UDE-based control of variable-speed wind turbine systems

Beibei Ren^a, Yeqin Wang^b and Qing-Chang Zhong^c

^aDepartment of Mechanical Engineering, Texas Tech University, Lubbock, TX, USA; ^bNational Wind Institute, Texas Tech University, Lubbock, TX, USA; ^cDepartment of Electrical and Computer Engineering, Illinois Institute of Technology, Chicago, IL, USA

ABSTRACT

In this paper, the control of a PMSG (permanent magnet synchronous generator)-based variable-speed wind turbine system with a back-to-back converter is considered. The uncertainty and disturbance estimator (UDE)-based control approach is applied to the regulation of the DC-link voltage and the control of the RSC (rotor-side converter) and the GSC (grid-side converter). For the rotor-side controller, the UDE-based vector control is developed for the RSC with PMSG control to facilitate the application of the MPPT (maximum power point tracking) algorithm for the maximum wind energy capture. For the grid-side controller, the UDE-based vector control is developed to control the GSC with the power reference generated by a UDE-based DC-link voltage controller. Compared with the conventional vector control, the UDE-based vector control can achieve reliable current decoupling control with fast response. Moreover, the UDE-based DC-link voltage regulation can achieve stable DC-link voltage under model uncertainties and external disturbances, e.g. wind speed variations. The effectiveness of the proposed UDE-based control approach is demonstrated through extensive simulation studies in the presence of coupled dynamics, model uncertainties and external disturbances under varying wind speeds. The UDE-based control is able to generate more energy, e.g. by 5% for the wind profile tested.

ARTICLE HISTORY

Received 9 February 2015
Accepted 27 November 2015

KEYWORDS

Wind turbine; UDE; vector control; current decoupling control; DC-link voltage regulation; model uncertainty; back-to-back converters

1. Introduction

Wind energy has been regarded as an environmentally friendly alternative energy source and has attracted most of attention (Zhong & Hornik, 2012). In contrast to fixed-speed wind turbines, variable-speed wind turbines are designed to follow wind speed variations in low winds to maximise aerodynamic efficiency, so they have the potential to produce more energy than fixed-speed ones (Ozbay, Zergeroglu, & Sivrioglu, 2008; Palejiya, Shaltout, Yan, & Chen, 2015). PMSG (permanent magnet synchronous generator) is one of the popular power generators in variable-speed wind turbine systems, as PMSG has excellent advantages, such as the elimination of DC excitation, high power density, high efficiency, and high reliability (Li, Haskew, Swatloski, & Gathings, 2012; Shariatpanah, Fadaeinedjad, & Rashidinejad, 2013; Zhang, Zhao, Qiao, & Qu, 2014).

In PMSG-based variable-speed wind turbine systems, full-scale back-to-back converters are often adopted for achieving maximum capture of wind power, providing low harmonic distortion of current, and operating the wind farm for provision of ancillary services (Seixas, Melicio, & Mendes, 2014; Zhong, Ma, Ming, & Konstantopoulos, 2015). The full-scale back-to-back

converters include a RSC (rotor-side converter) connected with the generator, a GSC (grid-side converter) connected to the grid, and a DC-link capacitor placed between the RSC and the GSC. The vector control, a conventional and classical control strategy based on the $d-q$ reference frame, is still applied in both the RSC for PMSG control and the GSC for power output control (Li et al., 2012; Shariatpanah et al., 2013; Yuan, Wang, Boroyevich, Li, & Burgos, 2009). However, the conventional vector control faces some difficulties, for example, it is sensitive to parameters tuning and uncertainty in the $d-q$ reference frame for current decoupling control (Zhong et al., 2015), the parameters tuning and uncertainty also reduce system stability and reliability (Li et al., 2012), the system response with current control is limited by time constant of the armature winding (Zhong, Rahman, Hu, & Lim, 1997), and the coupled current dynamics in $d-q$ reference frame enhance the difficulty of current regulation (Mohamed & Lee, 2006; Sneyers, Novotny, & Lipo, 1985). In recent years, the conventional vector control was improved by feed-forward compensation (Mohamed & Lee, 2006; Morimoto, Sanada, & Takeda, 1994) for current decoupling control, and hysteresis band PWM strategy (Rebeiro & Uddin, 2012) for nonlinear effect. The direct-current vector control

(Li et al., 2012) was proposed to enhance system stability, reliability and efficiency for PMSG-based wind turbines. The direct torque control was compared with conventional vector control for PMSM (permanent magnet synchronous motor) control to achieve fast system response (Zhong et al., 1997), and was also adopted in PMSG-based wind turbines (Haque, Saw, & Chowdhury, 2014; Zhang et al., 2014). The synchronverter technology was proposed for PMSG-based wind turbines system both on the RSC and the GSC in Zhong et al. (2015) to make the system more friendly to the grid, as synchronverter technology is independent to system parameters.

Although the back-to-back converters with vector control are widely used because it simplifies the control design, it has potential difficulties to achieve maximum wind power capture and DC-link voltage regulation for the whole wind turbine system, as the disturbance and uncertainties are difficult to handle (Chen, Yang, Guo, & Li, 2015; Li, Yang, Chen, & Chen, 2014). The wind turbines are large with flexible structures operating in noisy environments, and aerodynamic loads on the turbines are highly nonlinear (Johnson, Fingersh, Balas, & Pao, 2004; Leith & Leithead, 1997). The wind speed measurement on the nacelle is not suitable for feed forward control, and precise estimation of wind speed is very difficult (Soltani et al., 2013). The DC-link voltage is influenced by many factors, such as fluctuating power captured from wind, non-sinusoidal currents and reactive power delivered to the grid, and equivalent series resistance and inductance in the DC-link capacitor (Shariatpanah et al., 2013). In order to achieve the maximum wind power capture, some MPPT (maximum power point tracking) algorithms have been studied with fuzzy-logic-based control (Chedid, Karaki, & El-Chamali, 2000; Simoes, Bose, & Spiegel, 1997), wind speed estimation-based algorithm (Bhowmik, Spee, & Enslin, 1999) and optimal torque control (Morimoto, Nakayama, Sanada, & Takeda, 2005). Adaptive control scheme was proposed in Johnson et al. (2004) and Johnson, Pao, Balas, and Fingersh (2006) to deal with complex aerodynamics for MPPT. The conventional PI (proportional-integral) controller is still widely adopted in Shariatpanah et al. (2013), Li et al. (2012) and Zhong et al. (2015) for DC-link voltage regulation in wind turbine systems.

In this paper, a PMSG-based variable-speed wind turbine system with back-to-back converters is studied with the goals of maximum wind power capture and PMSG control in the rotor-side controller, and DC-link voltage regulation and power output control in the grid-side controller. To achieve these goals, the model of a PMSG-based variable-speed wind turbine with back-to-back converters is established at first, then the UDE (uncertainty and disturbance estimator)-based control

approach is applied for the RSC, the GSC and DC-link voltage regulation, respectively. The UDE algorithm, which was proposed in Zhong and Rees (2004), is based on the assumption that the uncertainty and disturbance can be estimated by using a filter with the appropriate bandwidth. In recent years, the UDE algorithm demonstrated excellent performance in handling uncertainties and disturbances in different systems, and was employed to robustify an input–output linearisation controller (Talole & Phadke, 2009; Talole, Chandar, & Kolhe, 2011) and input–output delay systems (Sun, Zhang, Li, Lee, & Zhang, 2015), and applied to robust trajectory tracking (Kolhe, Shaheed, Chandar, & Taloe, 2013), a class of non-affine nonlinear systems (Ren, Zhong, & Chen, 2015), three-DOF experimental helicopters (Zhu, Liu, & Li, 2015), piezoelectric actuator (Chen, Ren, & Zhong, 2015), and quadrotor vehicles (Sanz, Garcia, Zhong, & Albertos, 2015). In this paper, in the rotor-side controller, the optimal torque MPPT is first adopted for maximum wind energy capture, then the UDE-based vector control is developed for RSC with PMSG control to facilitate the application of the MPPT. In the grid-side controller, the UDE-based DC-link voltage regulation control is proposed to generate a power output reference, then the UDE-based vector control is developed for the GSC with power output control to facilitate the achievement of reliable DC-link voltage regulation. Compared with the conventional vector control, the UDE-based vector control can achieve the reliable current decoupling control in the d - q reference frame with fast response in varying wind speed conditions. And compared with the conventional PI controller, the UDE-based DC-link voltage regulation control can achieve the model uncertainty compensation and external disturbance rejection.

The main contributions of this paper are highlighted as follows:

- The UDE-based vector control is developed for both the RSC with PMSG control and the GSC with power output control to achieve reliable current decoupling control with fast response in varying wind speed conditions.
- Reliable DC-link voltage regulation control is developed based on the UDE algorithm to deal with model uncertainty, such as power losses, equivalent series resistance, equivalent series inductance and the reactive power on the capacitor, and external disturbances with varying wind speed conditions.

The effectiveness of the proposed UDE-based control approach is demonstrated through extensive simulation studies using the Matlab/Simulink/Simpowersystem. The comparison with the conventional PI control is also provided to show the robustness and higher energy capture of the proposed approach.

The rest of the paper is organised as follows. Section 2 briefly introduces mechanical part, electrical part and control part of a PMSG-based variable-speed wind turbine system with back-to-back converters. Section 3 details the modelling for this wind turbine system. The rotor-side controller is designed in Section 4 and the grid-side controller in Section 5. Effectiveness of the proposed approach is demonstrated through simulation studies in Section 6, before the concluding remarks are made in Section 7.

2. System description

Figure 1 shows a PMSG-based wind turbine system, which consists of three parts: mechanical part, electrical part and control part. In mechanical part, the rotational blades catch wind energy that is then transferred to the generator through a gear box. The gear box converts high-torque, low-speed mechanical power on the blade side to low-torque, high-speed mechanical power on the generator side. The generator, converting mechanical power into AC electrical power, is a standard surface-mounted PMSG with its stator windings connected to the RSC.

The electrical part is the standard back-to-back converters with one side connected to a generator and the other side connected to the grid. The RSC converts variable frequency AC power generated by PMSG to DC power fed into the GSC. The GSC converts the DC power to fixed frequency electricity that is compatible with the AC grid. And a DC-link capacitor is placed between the RSC and the GSC to smooth the DC-link voltage. Three-phase LC (inductor and capacitor) filters are added between the GSC and the grid to filter the PWM (pulse-width modulation) voltages generated by the GSC.

In this paper, a control structure as shown in Figure 1, including the rotor-side controller and the grid-side controller, is employed for the RSC and the GSC, respectively. The DC-link is the key linkage between the RSC and the GSC, and a stable DC-link voltage guarantees the stable operation of both the RSC and the GSC. The goals of the rotor-side controller are maximum power capture from the wind with the MPPT (maximum power point tracking) control algorithm, and converting AC power to DC power (the same as PMSG control) with the UDE-based vector control. The goals of the grid-side controller are keeping the DC-link voltage stable with the UDE-based DC-link voltage control, and converting DC power to grid AC power (the same as power output control) with the UDE-based vector control. For the grid-side controller, the UDE-based DC-link voltage regulation control regulates the DC-link voltage at a desired constant level through sending almost all the DC power generated by the RSC to the grid. As a result, a stable DC-link voltage is achieved.

3. System modelling

3.1 Wind power

The power produced by a wind turbine can be calculated as (Heier & Waddington, 1998)

$$P_m = \frac{1}{2} \rho \pi R^2 v_w^3 C_p(\lambda, \beta), \quad (1)$$

where ρ is the air density, R is the radius of the rotor, v_w is the wind speed, $C_p(\lambda, \beta)$ is the power coefficient that is dependent on the turbine design, β is the pitch angle, and

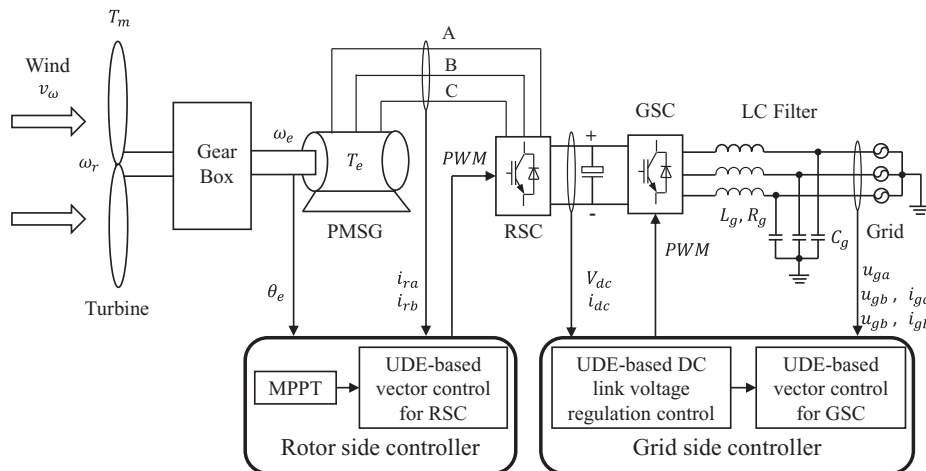


Figure 1. Schematic diagram of a PMSG-based wind turbine with back-to-back converters.

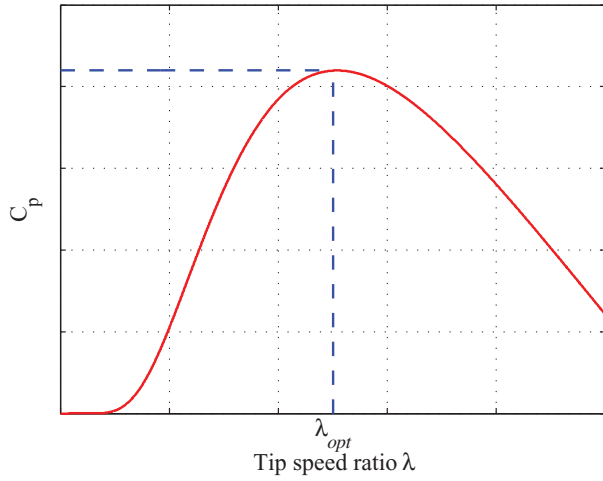


Figure 2. Power coefficient C_p as a function of the tip-speed ratio λ (Zhong & Hornik, 2012).

the tip-speed ratio λ is defined as

$$\lambda = \omega_r R / v_w, \quad (2)$$

where ω_r is the rotor speed of the wind turbine.

The power coefficient C_p is a highly nonlinear function of λ and β , which can be approximated as (Heier & Waddington, 1998)

$$C_p = c_1 \left(\frac{c_2}{\lambda_i} - c_3 \beta - c_4 \right) e^{-\frac{c_5}{\lambda_i}}, \quad (3)$$

with

$$\frac{1}{\lambda_i} = \frac{1}{\lambda + c_6} - \frac{c_7}{\beta^3 + 1},$$

where c_1 – c_7 are constant coefficients. For wind turbines with a fixed pitch angle β , the relationship between C_p and the tip speed ratio λ often has the shape shown in Figure 2.

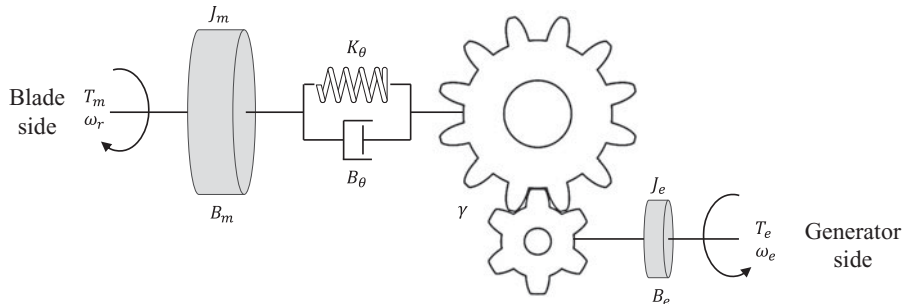


Figure 3. Mechanical scheme of the wind turbine transmission system.

3.2 Dynamic model of a PMSG-based wind turbine with back-to-back converters

Figure 1 shows the schematic diagram of a PMSG-based wind turbine with back-to-back converters where the RSC is connected with the generator and the GSC is connected with the grid. A DC-link capacitor is used between the RSC and the GSC to smooth the DC-link voltage.

3.2.1 Model of the PMSG-based wind turbine with the RSC

In Figure 1, the RSC is used to convert variable frequency AC power generated by PMSG to DC power fed into the GSC. As shown in Figure 3, the dynamics of the wind turbine transmission system (including the gear box, the shafts) between the blades and the generator are modelled as the spring damper model in Soltani et al. (2013):

$$J_m \dot{\omega}_r = T_m - K_\theta \theta - (B_m + B_\theta) \omega_r + \frac{B_\theta}{\gamma} \omega_e, \quad (4)$$

$$J_e \dot{\omega}_e = \frac{\eta_t K_\theta}{\gamma} \theta + \frac{\eta_t B_\theta}{\gamma} \omega_r - \left(\frac{\eta_t B_\theta}{\gamma^2} + B_e \right) \omega_e + T_e, \quad (5)$$

$$\dot{\theta} = \omega_r - \frac{1}{\gamma} \omega_e, \quad (6)$$

where J_m represents the moment of inertia of the blades and shaft on the low-speed blade side, B_m the viscous damper of main rotor bearing, and T_m the shaft torques at the blade end. Stiffness and damping of drive train are combined into one spring and one damper on blades side with coefficients K_θ and B_θ . J_e is the moment of inertia of the shaft, gear box and rotor of generator on the high-speed generator side, B_e is the friction-related damping constants in generator side. T_e is the electromagnetic torque of PMSG. η_t is the efficiency of the drive train. ω_r is the angular speed of the shaft at the blade end, ω_e is the angular speed of the shaft at the PMSG end, and θ_e is the corresponding electrical angle. θ is the shaft

torsion on the low-speed shaft. γ is the gear ratio of the gearbox.

It is well known that

$$T_m = \frac{P_m}{\omega_r}, \quad (7)$$

where P_m denotes the wind power given by (1).

The PMSG can be modelled in the a - b - c coordinates, α - β coordinates, or d - q coordinates, which can be linked through Clarke transformation or Park transformation. The PMSG model in the d - q coordinates are described as (Fitzgerald, Kingsley, & Umans, 2003)

$$U_{sd} = L_{sd}\dot{i}_{rd} + R_s i_{rd} - p\omega_e L_{sq} i_{rq}, \quad (8)$$

$$U_{sq} = L_{sq}\dot{i}_{rq} + R_s i_{rq} + p\omega_e L_{sd} i_{rd} + p\omega_e \psi_f, \quad (9)$$

where U_{sd} and U_{sq} represent the stator voltages, i_{rd} and i_{rq} are the stator currents, R_s represents the stator winding resistance, L_{sd} and L_{sq} represent the stator winding inductance, p is the number of pole pairs, and ψ_f is the core magnetic flux.

The electromagnetic torque T_e of the PMSG can be calculated as

$$T_e = \frac{3}{2}p[\psi_f i_{rq} - (L_{sq} - L_{sd})i_{rd} i_{rq}]. \quad (10)$$

As the PMSG is considered as the surface-mounted magnet type, L_{sd} and L_{sq} are equal. Then, $i_{rd} = 0$ control can be adopted for the torque control and T_e in (10) can be reduced to

$$T_e = \frac{3}{2}p\psi_f i_{rq}, \quad (11)$$

which indicates that the torque output T_e of PMSG can be controlled through the adjustment of the q -axis current i_{rq} directly.

3.2.2 Model of the GSC with the DC-link and the grid

In Figure 1, the GSC is used to absorb the DC power from the RSC and convert it to the AC grid power. A DC-link capacitor between the RSC and the GSC is used to balance the DC-link voltage. However, the DC-link capacitor can only filter high-order fluctuation on the RSC and the GSC sides. In order to keep the DC-link voltage stable, the power coming out of the DC-link capacitor should be equal to the power injected into the capacitor. In order to filter the PWM (pulse-width modulation) noise on the grid side, three-phase LC (inductors and capacitors) filters are also added between the GSC and the grid.

The full DC-link dynamics are very complex and cannot be used for control directly (Shariatpanah et al., 2013).

A DC-link voltage equation simplified from Shariatpanah et al. (2013) with unknown parameters is shown as

$$\dot{V}_{dc} = \frac{P_{in}}{CV_{dc}} - \frac{P_{out}}{CV_{dc}} - \frac{P_{loss}}{CV_{dc}} + \Delta_{v0}, \quad (12)$$

where V_{dc} is the DC-link voltage, C is the capacitance value of the DC-link capacitor, P_{in} represents the DC power from the RSC, P_{out} represents the real power output of the GSC, P_{loss} denotes the power losses on the DC-link capacitor and the GSC, and Δ_{v0} represents the effects of unknown parameters, such as equivalent series resistance, equivalent series inductance and the reactive power. The DC-link dynamics (12) show that the DC-link voltage V_{dc} can be controlled through the adjustment of the real power output P_{out} of the GSC. Normally, P_{in} can be measured directly, but P_{loss} and Δ_{v0} are difficult to be measured directly.

Similar to the PMSG modelling in the d - q coordinates, the three-phase grid also can be modelled in the d - q coordinates as Shariatpanah et al. (2013)

$$U_{gd} = L_g \dot{i}_{gd} + R_g i_{gd} - \omega_g L_g i_{gq} + u_{gd}, \quad (13)$$

$$U_{gq} = L_g \dot{i}_{gq} + R_g i_{gq} + \omega_g L_g i_{gd} + u_{gq}, \quad (14)$$

where U_{gd} and U_{gq} represent the output voltages of the GSC, i_{gd} and i_{gq} are the output currents of the GSC, R_g and L_g represent the line resistance and inductance, u_{gd} and u_{gq} are the grid voltage, ω_g is the grid frequency, and the corresponding phase angle θ_g can be calculated by a PLL (phase-locked-loop). Note that the capacitance C_g of the filter capacitors in Figure 1 is very small and only used for filtering the high-order noise, which can be ignored in the modelling for simplification.

The instantaneous real power output P_{out} and reactive power output Q_{out} generated from the GSC are defined as

$$P_{out} = U_{gd} i_{gd} + U_{gq} i_{gq}, \quad (15)$$

$$Q_{out} = U_{gd} i_{gq} + U_{gq} i_{gd}. \quad (16)$$

For the real power P_{out} output control of the GSC, $i_{gq} = 0$ control is often adopted in the vector control. Then, (15) and (16) can be simplified as

$$P_{out} = U_{gd} i_{gd}, \quad (17)$$

$$Q_{out} = U_{gq} i_{gd}. \quad (18)$$

4. Design of the rotor-side controller

The control scheme of rotor-side controller (shown in Figure 4) is developed to achieve maximum wind power capture and PMSG control. In the outer loop, the MPPT control algorithm is adopted to generate a torque reference T_e^* . In the inner loop, the UDE-based vector control is developed to control the currents i_{rd} and i_{rq} to achieve the PMSG torque control and convert AC power to DC power simultaneously.

4.1 MPPT control without wind speed information

It is well known that there are four wind speed regions for wind turbine control (Wu, Lang, Zargari, & Kouro, 2011). In Region I, the wind speed is lower than the cut-in speed and the wind turbine is closed; in Region II, MPPT control is adopted to extract the maximum wind power at different wind speeds through keeping the optimal tip-speed ratio λ_{opt} ; in Region III, the wind speed is higher than the rated wind speed and the pitch control is adopted to keep constant power generation; in Region IV, the wind speed is higher than the cut-off speed and full pitch control is adopted to protect the wind turbine. In this work, it is assumed that the wind turbine is operated in Region II to extract the maximum power from the wind. In the outer loop of the rotor-side controller shown in Figure 4, the optimal torque MPPT algorithm in Morimoto et al. (2005) is adopted to catch the maximum power via adjusting the tip-speed ratio λ in (2) without the wind speed information, as the precise estimation of wind speed is very difficult (Soltani et al., 2013).

As the power coefficient C_p is a nonlinear function of λ and β , there is an optimal tip-speed ratio λ_{opt} to achieve the optimal power coefficient C_{p_opt} for a constant β . According to (1) and (7), the optimal torque T_{m_opt} can be expressed as

$$T_{m_opt} = K_{opt} \omega_{r_opt}^2, \quad (19)$$

where

$$K_{opt} = \frac{\rho \pi C_{p_opt} R^5}{2 \lambda_{opt}^3}. \quad (20)$$

According to (2), the optimal blade shaft speed ω_{r_opt} satisfies

$$\omega_{r_opt} = \frac{\lambda_{opt} v_\omega}{R}.$$

Replacing ω_{r_opt} with the blade shaft speed ω_r in (19) and considering (4)–(6) with the steady angular speed of the shaft, steady generator speed and steady shaft torsion

$$\dot{\omega}_r = 0, \quad \dot{\omega}_e = 0, \quad \dot{\theta} = 0,$$

the generator torque reference by the PMSG can be expressed as

$$T_e^* = -\frac{\eta_t K_{opt} \omega_e^2}{\gamma^3} + \frac{\eta_t B_m \omega_e}{\gamma^2} + B_e \omega_e.$$

Here, the generator speed ω_e is usually adopted to replace the blade shaft speed ω_r for the torque MPPT algorithm, as ω_e is easy to obtain.

Usually, the mechanical losses of drive train in (5) can be ignored with $\eta_t = 1$ as it is very small. The reference torque can be reduced to

$$T_e^* = -\frac{K_{opt} \omega_e^2}{\gamma^3} + \frac{B_m \omega_e}{\gamma^2} + B_e \omega_e. \quad (21)$$

4.2 UDE-based vector control for RSC-PMSG

In Figure 4, the control objective of the inner loop on the rotor-side controller is to make the torque output of PMSG to follow the torque reference T_e^* in (21) through regulating the PMSG currents in the d - q coordinates. In particular, the tracking errors $e_{ird} = i_{rd}^* - i_{rd}$ and $e_{irq} = i_{rq}^* - i_{rq}$ are specified to satisfy the following dynamics:

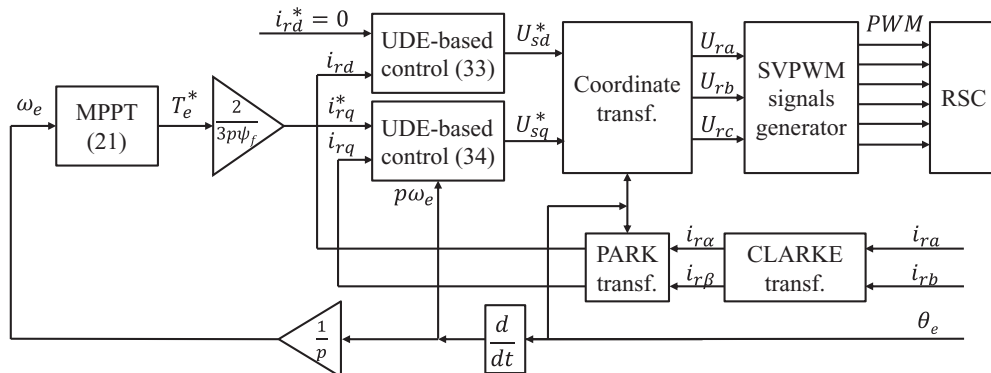


Figure 4. The proposed control scheme on the rotor-side controller.

$$\dot{e}_{ird} = -K_{ird}e_{ird}, \quad (22)$$

$$\dot{e}_{irq} = -K_{irq}e_{irq}. \quad (23)$$

It is noted that in the PMSG model (8) and (9), there are coupled current dynamics in the d - q coordinates, which enhance the difficulty of current regulation in the vector control. In this work, the coupled current dynamics will be regarded as the disturbance terms and handled by the UDE-based current decoupling control. To facilitate the control design, the PMSG models (8) and (9) can be rewritten as

$$U_{sd}^* = L_{sd}\dot{i}_{rd} + R_s i_{rd} + \Delta_{ird}, \quad (24)$$

$$U_{sq}^* = L_{sq}\dot{i}_{rq} + R_s i_{rq} + p\omega_e \psi_f + \Delta_{irq}, \quad (25)$$

where $\Delta_{ird} = -p\omega_e L_{sq} i_{rq}$, $\Delta_{irq} = p\omega_e L_{sd} i_{rd}$ represent the coupled terms, which are treated as uncertainties. Combining Equations (24) and (22) and combining Equations (25) and (23), then

$$\begin{aligned} \dot{i}_{rd}^* + \frac{R_s}{L_{sd}} i_{rd} - \frac{U_{sd}^*}{L_{sd}} + \frac{\Delta_{ird}}{L_{sd}} &= -K_{ird} e_{ird}, \\ \dot{i}_{rq}^* + \frac{R_s}{L_{sq}} i_{rq} - \frac{U_{sq}^*}{L_{sq}} + \frac{p\omega_e \psi_f}{L_{sq}} + \frac{\Delta_{irq}}{L_{sq}} &= -K_{irq} e_{irq}. \end{aligned}$$

So, the stator voltage references U_{sd}^* and U_{sq}^* need to satisfy

$$U_{sd}^* = L_{sd}\dot{i}_{rd}^* + R_s i_{rd} + L_{sd}K_{ird}e_{ird} + \Delta_{ird}, \quad (26)$$

$$U_{sq}^* = L_{sq}\dot{i}_{rq}^* + R_s i_{rq} + p\omega_e \psi_f + L_{sq}K_{irq}e_{irq} + \Delta_{irq}. \quad (27)$$

According to the system dynamics in (24) and (25), the uncertainty terms can be represented as

$$\begin{aligned} \Delta_{ird} &= U_{sd}^* - L_{sd}\dot{i}_{rd} - R_s i_{rd}, \\ \Delta_{irq} &= U_{sq}^* - L_{sq}\dot{i}_{rq} - R_s i_{rq} - p\omega_e \psi_f. \end{aligned}$$

Following the procedures provided in Zhong and Rees (2004), it is assumed that $g_{irdf}(t)$ and $g_{irqf}(t)$ are the impulse response of strictly proper stable filters $G_{irdf}(s)$ and $G_{irqf}(s)$ with appropriate frequency characteristics over the spectrum of Δ_{ird} and Δ_{irq} , respectively. Then, Δ_{ird} and Δ_{irq} can be accurately approximated by

$$\hat{\Delta}_{ird} = \Delta_{ird} * g_{irdf} = (U_{sd}^* - L_{sd}\dot{i}_{rd} - R_s i_{rd}) * g_{irdf}, \quad (28)$$

$$\begin{aligned} \hat{\Delta}_{irq} &= \Delta_{irq} * g_{irqf} = (U_{sq}^* - L_{sq}\dot{i}_{rq} - R_s i_{rq} \\ &\quad - p\omega_e \psi_f) * g_{irqf}, \end{aligned} \quad (29)$$

where $\hat{\Delta}_{ird}$ is an estimate of Δ_{ird} , and $\hat{\Delta}_{irq}$ is an estimate of Δ_{irq} . Replacing Δ_{ird} with $\hat{\Delta}_{ird}$, and Δ_{irq} with $\hat{\Delta}_{irq}$, respectively, in (26) and (27) results in

$$\begin{aligned} U_{sd}^* &= L_{sd}\dot{i}_{rd}^* + R_s i_{rd} + L_{sd}K_{ird}e_{ird} \\ &\quad + (U_{sd}^* - L_{sd}\dot{i}_{rd} - R_s i_{rd}) * g_{irdf}, \\ U_{sq}^* &= L_{sd}\dot{i}_{rq}^* + R_s i_{rq} + p\omega_e \psi_f + L_{sq}K_{irq}e_{irq} \\ &\quad + (U_{sq}^* - L_{sq}\dot{i}_{rq} - R_s i_{rq} - p\omega_e \psi_f) * g_{irqf}. \end{aligned}$$

These result in the UDE-based control laws

$$\begin{aligned} U_{sd}^* &= R_s i_{rd} + L^{-1} \left\{ \frac{1}{1 - G_{irdf}(s)} \right\} * (L_{sd}\dot{i}_{rd}^* + L_{sd}K_{ird}e_{ird}) \\ &\quad - L^{-1} \left\{ \frac{sG_{irdf}(s)}{1 - G_{irdf}(s)} \right\} * (L_{sd}\dot{i}_{rd}), \end{aligned} \quad (30)$$

$$\begin{aligned} U_{sq}^* &= R_s i_{rq} + p\omega_e \psi_f + L^{-1} \left\{ \frac{1}{1 - G_{irqf}(s)} \right\} \\ &\quad * (L_{sd}\dot{i}_{rq}^* + L_{sq}K_{irq}e_{irq}) \\ &\quad - L^{-1} \left\{ \frac{sG_{irqf}(s)}{1 - G_{irqf}(s)} \right\} * (L_{sq}\dot{i}_{rq}). \end{aligned} \quad (31)$$

The filter design is very important in the UDE algorithm, as the filter should cover the spectrum of disturbances with the unity gain and zero phase shift. Different choices of filters will result in different forms of UDE controller, which depends on system dynamics and performance requirements. In this paper, it is sufficient to choose $G_{irdf}(s)$ and $G_{irqf}(s)$ as the following first-order low-pass filters:

$$G_{irdf}(s) = \frac{1}{1 + \tau_{ird}s}, \quad G_{irqf}(s) = \frac{1}{1 + \tau_{irq}s}. \quad (32)$$

Then,

$$\frac{1}{1 - G_{irdf}(s)} = 1 + \frac{1}{\tau_{ird}s}, \quad \frac{1}{1 - G_{irqf}(s)} = 1 + \frac{1}{\tau_{irq}s},$$

and

$$\frac{sG_{irdf}(s)}{1 - G_{irdf}(s)} = \frac{1}{\tau_{ird}}, \quad \frac{sG_{irqf}(s)}{1 - G_{irqf}(s)} = \frac{1}{\tau_{irq}}.$$

Therefore, the UDE-based control laws (30) and (31) are calculated as

$$\begin{aligned} U_{sd}^* &= R_s i_{rd} + L_{sd}\dot{i}_{rd}^* + \frac{L_{sd}}{\tau_{ird}} (1 + \tau_{ird}K_{ird})e_{ird} \\ &\quad + \frac{L_{sd}K_{ird}}{\tau_{ird}} \int_0^t e_{ird} dt, \\ U_{sq}^* &= R_s i_{rq} + L_{sd}\dot{i}_{rq}^* + p\omega_e \psi_f \\ &\quad + \frac{L_{sq}}{\tau_{irq}} (1 + \tau_{irq}K_{irq})e_{irq} + \frac{L_{sq}K_{irq}}{\tau_{irq}} \int_0^t e_{irq} dt. \end{aligned}$$

From Figure 4, it can be seen that i_{rq}^* is generated from the torque reference T_e^* where the relationship between i_{rq}^* and T_e^* is shown in (11). Since the surface-mounted magnet type of PMSG is considered, i_{rd}^* is set to zero, and its derivative is also zero. Then, the UDE-based control laws are reduced to

$$U_{sd}^* = R_s i_{rd} + \frac{L_{sd}}{\tau_{ird}} (1 + \tau_{ird} K_{ird}) e_{ird} + \frac{L_{sd} K_{ird}}{\tau_{ird}} \int_0^t e_{ird} dt, \quad (33)$$

$$U_{sq}^* = R_s i_{rq} + L_{sd} \dot{i}_{rq}^* + p\omega_e \psi_f + \frac{L_{sq}}{\tau_{irq}} (1 + \tau_{irq} K_{irq}) e_{irq} + \frac{L_{sq} K_{irq}}{\tau_{irq}} \int_0^t e_{irq} dt, \quad (34)$$

where the currents i_{rd} and i_{rq} can be obtained from three-phase currents i_{ra} and i_{rb} through the Clarke transformation and Park transformation as shown in Figure 4. The outputs of the above UDE-based control laws, U_{sd}^* and U_{sq}^* , are converted to six SVPWM (space-vector pulse width modulation) signals to drive power electronics of the RSC through a coordinate transformation and a SVPWM generation module. The details about the vector control can be found in Sul (2011).

5. Design of the grid-side controller

In order to achieve the DC-link voltage regulation and power output control, the control scheme of grid-side controller is shown in Figure 5. In the outer loop of the grid-side controller, the DC-link voltage regulation with the UDE algorithm is designed to generate a real power output reference P_{out}^* . In the inner loop of the grid-side controller, the UDE-based vector control is developed to regulate the currents i_{gd} and i_{gq} to achieve real power output control and convert DC power to grid AC power simultaneously.

5.1 UDE-based DC-link voltage regulation

For the grid-side controller, the control objective of the outer loop in Figure 5 is to generate a real power output reference P_{out}^* such that the DC-link voltage V_{dc} in (12) asymptotically tracks a reference voltage V_0 , in particular, the tracking error $e_v = V_0 - V_{dc}$ asymptotically converges to zero by following the desired error dynamics

$$\dot{e}_v = -K_v e_v, \quad (35)$$

where K_v is an error feedback gain. Instead of the nominal model (12), the following modified model is considered

in the presence of the uncertainties and disturbances:

$$\dot{V}_{dc} = \frac{P_{in}}{CV_0} - \frac{P_{out}^*}{CV_0} + \Delta_v, \quad (36)$$

where V_0 is a constant reference value for V_{dc} , and Δ_v represents the lumped uncertainty and disturbance term $\Delta_v = \frac{P_{in}}{CV_{dc}} - \frac{P_{out}}{CV_{dc}} - \frac{P_{loss}}{CV_{dc}} + \Delta_{v0} - \frac{P_{in}}{CV_0} + \frac{P_{out}}{CV_0}$. In the normal operation condition, the DC-link voltage V_{dc} should be close to V_0 .

Combining Equations (35) and (36), there is

$$\dot{V}_0 - \frac{P_{in}}{CV_0} + \frac{P_{out}^*}{CV_0} - \Delta_v = -K_v e_v.$$

The real power output reference P_{out}^* needs to satisfy

$$P_{out}^* = -CV_0 \dot{V}_0 + P_{in} + CV_0 \Delta_v - CV_0 K_v e_v. \quad (37)$$

According to the system dynamics in (36), Δ_v can be represented as

$$\Delta_v = \dot{V}_{dc} - \frac{P_{in}}{CV_0} + \frac{P_{out}^*}{CV_0}.$$

Assume that $g_{vf}(t)$ is the impulse response of a strictly proper stable filter $G_{vf}(s)$ with the appropriate frequency characteristics over the spectrum of Δ_v . Following the similar procedures in Section 4.2, the UDE-based control law can be expressed as

$$P_{out}^* = P_{in} + CV_0 \left[L^{-1} \left\{ \frac{1}{1 - G_{vf}(s)} \right\} * (-K_v e_v) + L^{-1} \left\{ \frac{sG_{vf}(s)}{1 - G_{vf}(s)} \right\} * V_{dc} \right]. \quad (38)$$

If the filter $G_{vf}(s)$ is chosen as the following first-order low-pass filter:

$$G_{vf}(s) = \frac{1}{1 + \tau_v s},$$

the UDE-based control law (38) is derived as follows:

$$P_{out}^* = P_{in} - CV_0 \dot{V}_0 - \frac{CV_0}{\tau_v} \left[(K_v \tau_v + 1) e_v + K_v \int_0^t e_v dt \right].$$

Considering V_0 as a constant value, $\dot{V}_0 = 0$. Then, the UDE-based control law can be reduced to

$$P_{out}^* = P_{in} - \frac{CV_0}{\tau_v} \left[(K_v \tau_v + 1) e_v - K_v \int_0^t e_v dt \right]. \quad (39)$$

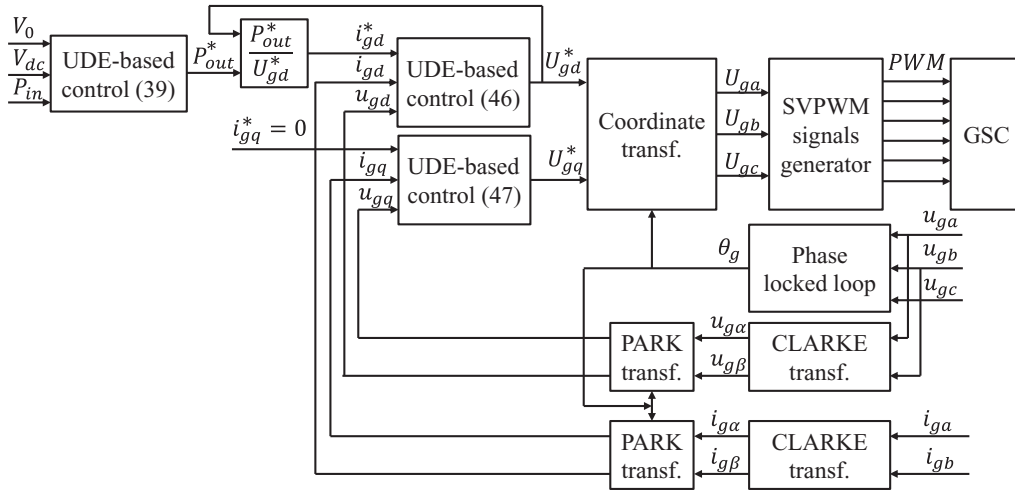


Figure 5. The proposed control scheme for the grid-side controller.

5.2 UDE-based vector control for GSC with real power output control

In Section 5.1, the UDE-based DC-link voltage regulation control is used to generate a real power output reference P_{out}^* in (39) of the grid-side controller to achieve the DC-link voltage regulation. Similar to the modified vector control of PMSG in Section 4.2, in this section, the UDE-based vector control is developed to achieve the GSC real power output control by adjusting the current i_{gd} as shown in Figure 5.

The objective is to make the grid currents track the reference currents in d - q coordinates which are obtained by the real power output reference P_{out}^* , and the tracking errors $e_{igd} = i_{gd}^* - i_{gd}$, $e_{igq} = i_{gq}^* - i_{gq}$ asymptotically converge to zero with the desired error dynamics specified as

$$\dot{e}_{igd} = -K_{igd}e_{igd}, \quad (40)$$

$$\dot{e}_{igq} = -K_{igq}e_{igq}. \quad (41)$$

Similar to the voltage equations of PMSG, the current coupling items in Equations (13) and (14) can be represented as uncertainty terms $\Delta_{igd} = -\omega_g L_g i_{gq}$, $\Delta_{igq} = \omega_g L_g i_{gd}$ to facilitate the current decoupling control of i_{gd} and i_{gq} as

$$U_{gd} = L_g \dot{i}_{gd} + R_g i_{gd} + u_{gd} + \Delta_{igd}, \quad (42)$$

$$U_{gq} = L_g \dot{i}_{gq} + R_g i_{gq} + u_{gq} + \Delta_{igq}. \quad (43)$$

Following the similar procedures of the UDE-based control in Section 4.2, the control laws can be obtained as

$$U_{gd}^* = R_g i_{gd} + u_{gd} + L^{-1} \left\{ \frac{1}{1 - G_{igdf}(s)} \right\} * (L_g \dot{i}_{gd}^* + L_g K_{igd} e_{igd}) - L^{-1} \left\{ \frac{s G_{irdf}(s)}{1 - G_{irdf}(s)} \right\} * (L_g i_{gd}), \quad (44)$$

$$U_{gq}^* = R_g i_{gq} + u_{gq} + L^{-1} \left\{ \frac{1}{1 - G_{igqf}(s)} \right\} * (L_g \dot{i}_{gq}^* + L_g K_{igq} e_{igq}) - L^{-1} \left\{ \frac{s G_{irqf}(s)}{1 - G_{irqf}(s)} \right\} * (L_g i_{gq}), \quad (45)$$

where $g_{igdf}(t)$ and $g_{igqf}(t)$ are the impulse response of strictly proper stable filters $G_{igdf}(s)$ and $G_{igqf}(s)$ with appropriate frequency characteristics over the spectrum of Δ_{igd} and Δ_{igq} , respectively. When both filters $G_{igdf}(s)$ and $G_{igqf}(s)$ are designed as the following first-order low-pass filters

$$G_{igdf}(s) = \frac{1}{1 + \tau_{igd}s}, \quad G_{igqf}(s) = \frac{1}{1 + \tau_{igq}s},$$

the UDE-based control laws (44) and (45) can be obtained as

$$U_{gd}^* = R_g i_{gd} + u_{gd} + L_g \dot{i}_{gd}^* + \frac{L_g}{\tau_{igd}} (1 + \tau_{igd} K_{igd}) e_{igd} + \frac{L_g K_{igd}}{\tau_{igd}} \int_0^t e_{igd} dt,$$

$$U_{gq}^* = R_g i_{gq} + u_{gq} + L_g \dot{i}_{gq}^* + \frac{L_g}{\tau_{igq}} (1 + \tau_{igq} K_{igq}) e_{igq} + \frac{L_g K_{igq}}{\tau_{igq}} \int_0^t e_{igq} dt.$$

From Figure 5, it can be seen that i_{gd}^* is generated from the real power output reference P_{out}^* where the relationship between i_{gd}^* and P_{out}^* is shown in (17). i_{gd}^* is set to zero, and its derivative is also zero. Then, the UDE-based control laws can be reduced to

$$U_{gd}^* = R_g i_{gd} + u_{gd} + L_g \dot{i}_{gd} + \frac{L_g}{\tau_{igd}} (1 + \tau_{igd} K_{igd}) e_{igd} + \frac{L_g K_{igd}}{\tau_{igd}} \int_0^t e_{igd} dt, \quad (46)$$

$$U_{gq}^* = R_g i_{gq} + u_{gq} + L_g \dot{i}_{gq} + \frac{L_g}{\tau_{igq}} (1 + \tau_{igq} K_{igq}) e_{igq} + \frac{L_g K_{igq}}{\tau_{igq}} \int_0^t e_{igq} dt. \quad (47)$$

It is worth noting that the minimal value of U_{gd}^* is the u_{gq} , which can be measured as shown in Figure 5. So, U_{gd}^* is non-zero and can be used as a denominator in Figure 5 to generate i_{gd}^* . Then, U_{gd}^* and U_{gq}^* are adopted to generate the SVPWM signals to drive power electronics of the GSC.

6. Simulation studies

6.1 With the proposed UDE-based control approach

In this section, simulation results are presented to verify the effectiveness of the proposed UDE-based

Table 1. System parameters.

Parameters	Values	Unit
J_m	3	kg m ²
J_e	0.01	kg m ²
K_θ	2×10^5	Nm/rad
B_m	37	Nm/rad/s
B_θ	0.02	Nm/rad/s
B_e	0.01	Nm/rad/s
γ	37.5	–
R	2.5	m
ρ	1.2	kg m ³
R_s	0.03	Ω
L_{sd}, L_{sq}	6.365	mH
ψ_f	0.192	V s
p	4	–
C	1000	μ F
L_g	4.4	mH
R_g	0.10	Ω
C_g	22	μ F

control approach through the Matlab/Simulink/Simpowersystem. All simulations in this paper are studied when the wind turbine is operated in Region II. The parameters of the PMSG-based wind turbine system with back-to-back converters under study are given in Table 1 (Ren & Zhong, 2013; Shariatpanah et al., 2013; Song, Dhinakaran, & Bao, 2000). The amplitude and frequency of the grid voltage are set as 380 V_{rms} and 50 Hz, respectively. The DC-link voltage reference V_0 is 600 V. The wind speed is chosen as the sum of

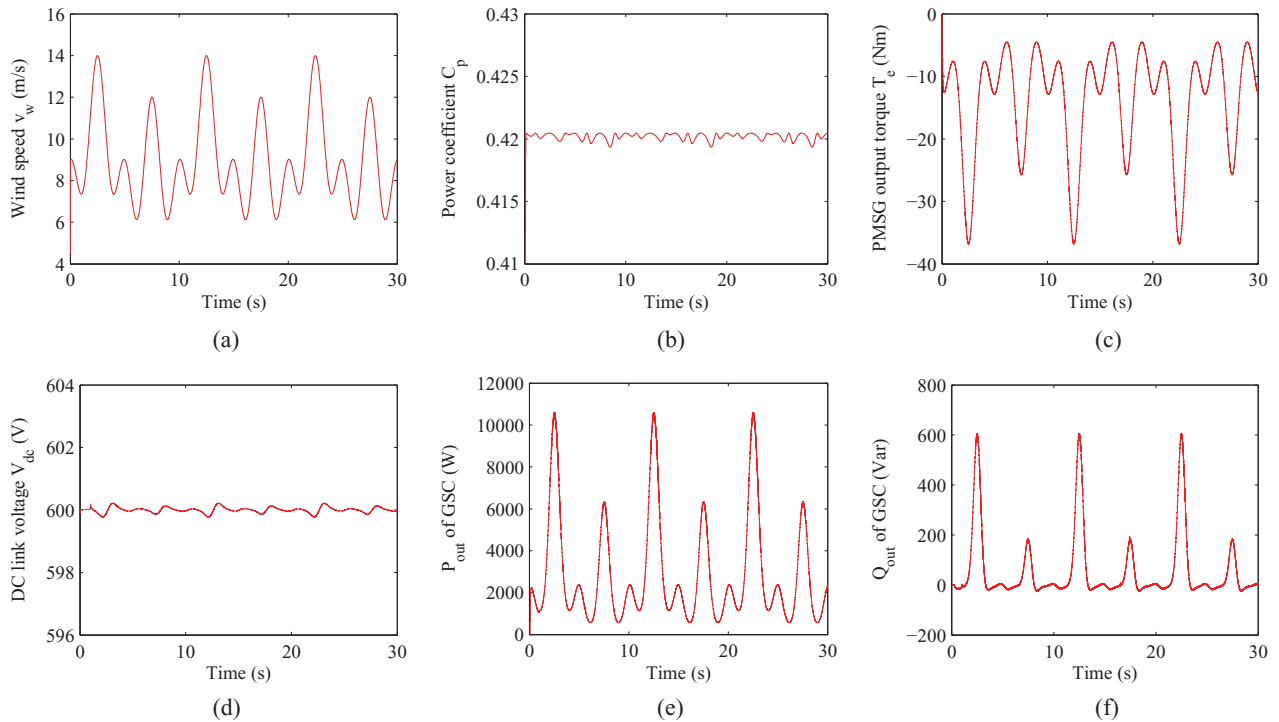


Figure 6. System performance. (a) Wind speed. (b) Power coefficient. (c) PMSG output torque. (d) DC-link voltage. (e) Real power output of the GSC. (f) Reactive power output of the GSC.

one constant signal and several sinusoidal signals $v_w = [9 + \sin(0.2\pi t) + 2*\sin(0.4\pi t - \pi/2) + 2*\sin(0.8\pi t + \pi/2)]$ (m/s) with the variation range of ± 4 m/s. The power coefficient C_p in (3) is chosen as

$$C_p = 0.545 \left[\frac{19}{\lambda} (1 - 0.03\lambda) - 7 \right] e^{-(\frac{3}{\lambda} - 0.09)}$$

with pitch angle $\beta = 0$. C_p reaches the maximum value with $C_{p-opt} = 0.4205$ when $\lambda_{opt} = 1.37$. The control parameters used in the rotor-side controller and the grid-side controller are provided in Tables 2 and 3, respectively.

The system performance is shown in Figure 6. The wind speed is plotted in Figure 6(a). The corresponding power coefficient is shown in Figure 6(b) and the output

Table 2. Parameters of the rotor-side controller.

Parameters	Values	Parameters	Values
K_{opt}	30.07	K_{irq}	40
K_{ird}	40	τ_{irq}	0.0001 s
τ_{ird}	0.0001 s	—	—

Table 3. Parameters of the grid-side controller.

Parameters	Values	Parameters	Values
K_v	10	τ_{igd}	0.0005 s
τ_v	0.001 s	K_{igq}	40
K_{igd}	40	τ_{igq}	0.0005 s

torque of PMSG is plotted in Figure 6(c). It can be seen that the power coefficient C_p can almost keep to the maximum value 0.4205, and the trend of the output torque of

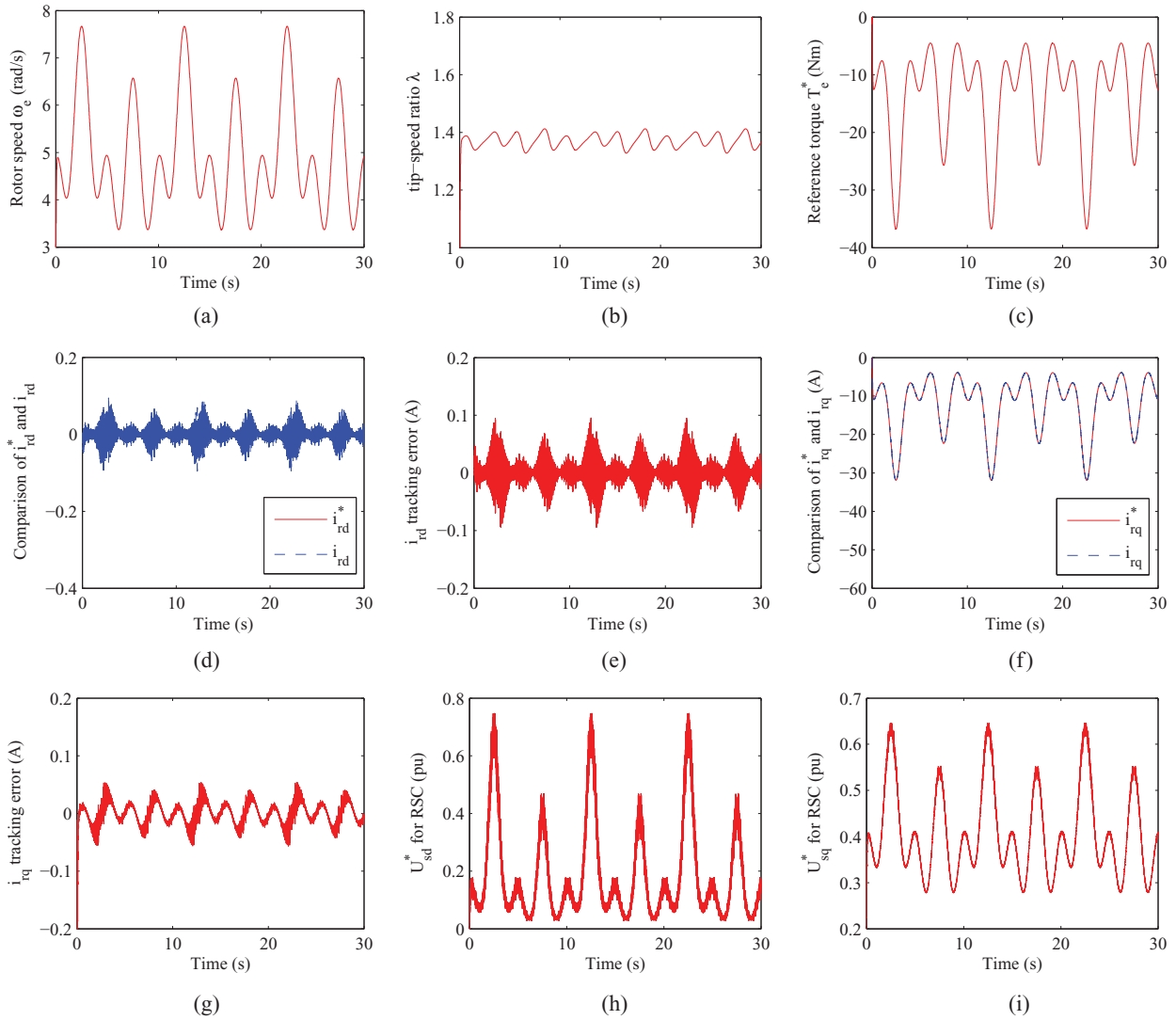


Figure 7. Simulation results on the rotor side. (a) Rotor speed. (b) Tip-speed ratio. (c) PMSG reference torque. (d) d -axis stator current. (e) d -axis stator current tracking error. (f) q -axis stator current. (g) q -axis stator current tracking error. (h) d -axis stator voltage reference. (i) q -axis stator voltage reference.

PMSG follows the trend of the wind speed well. Both of them verify the effectiveness of the MPPT control algorithm and the proposed UDE-based vector control for the rotor-side controller. The small fluctuation of C_p is caused by dynamic turning of the output torque of PMSG due to the big variation of wind speed. The DC-link voltage is shown in Figure 6(d), which is maintained around the target value 600 V under varying wind speed conditions, and the trend of real power output of the GSC shown in Figure 6(e) also follows the trend of the wind speed well. Both of them verify the effectiveness of the proposed UDE-based DC-link voltage regulation control and the UDE-based vector control in the grid-side controller. The reactive power output of the GSC is shown in Figure 6(f). It can be seen that Q_{out} has some fluctuation, which is reasonable as the $i_{gq} = 0$ control is adopted here.

The detailed simulation results for the rotor side are shown in Figure 7. The rotor speed is plotted in Figure 7(a), where the trend of rotor speed follows the wind speed in Figure 6(a) well. The tip-speed ratio almost keeps to the optimal value $\lambda_{opt} = 1.37$, which also shows the maximum wind power is captured. The torque reference T_e^* generated by the MPPT control algorithm is shown in Figure 7(c), which is very close to PMSG output torque T_e in Figure 6(c). The tracking performance of the stator currents in d - q axes are shown in Figure 7(d)–(g). The tracking errors are within $\pm 1\%$, which indicates that the UDE-based vector control is very effective to achieve the current decoupling control and achieve the good tracking performance. The corresponding voltage references U_{sd}^* and U_{sq}^* are shown in Figure 7(h) and 7(i). The trends of U_{sd}^* and U_{sq}^* look the same. However, the aim

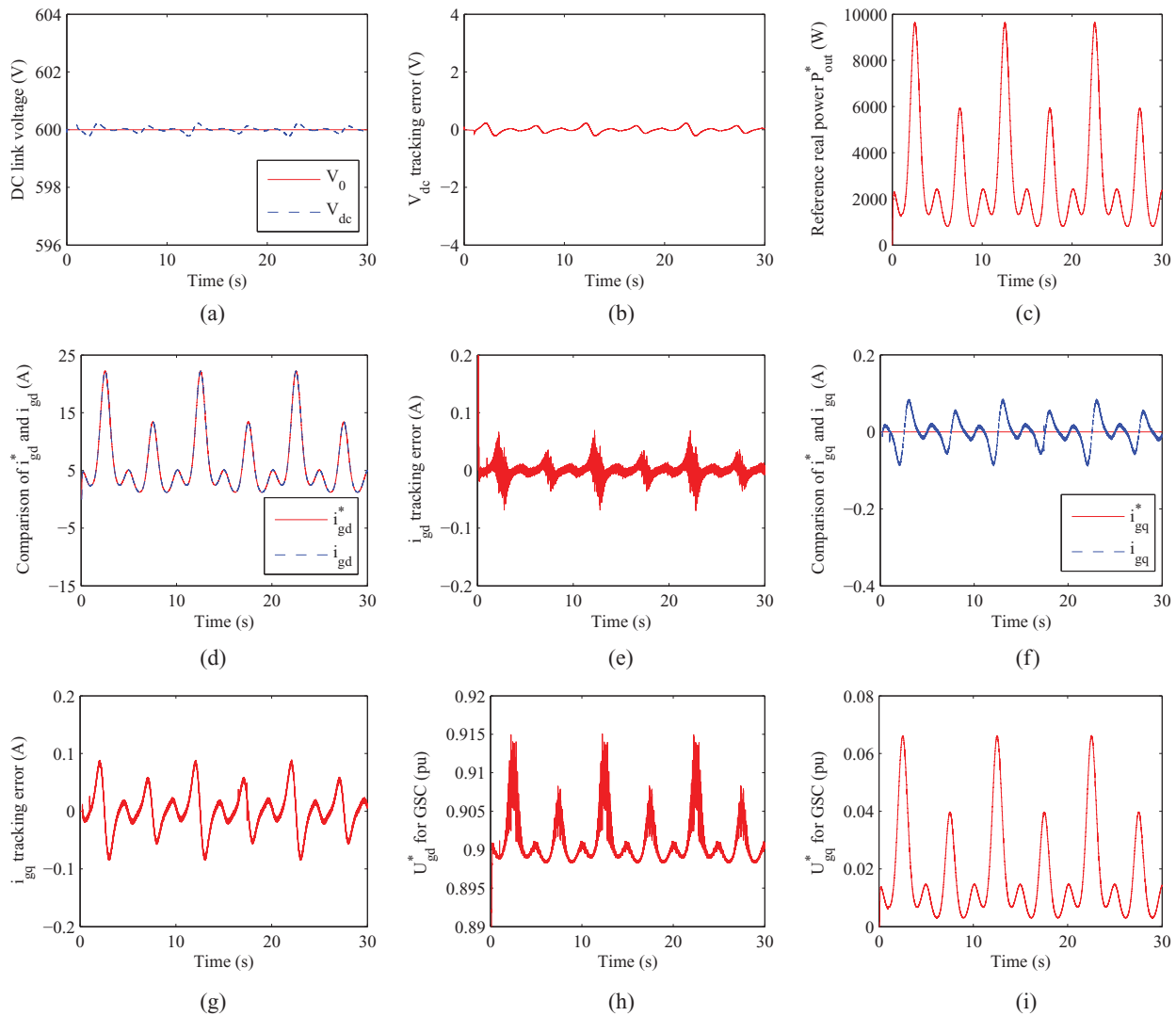


Figure 8. Simulation results on the grid side. (a) DC-link voltage. (b) DC-link voltage tracking error. (c) Real power output reference. (d) d -axis grid current. (e) d -axis grid current tracking error. (f) q -axis grid current. (g) q -axis grid current tracking error. (h) d -axis GSC output voltage reference. (i) q -axis GSC output voltage reference.

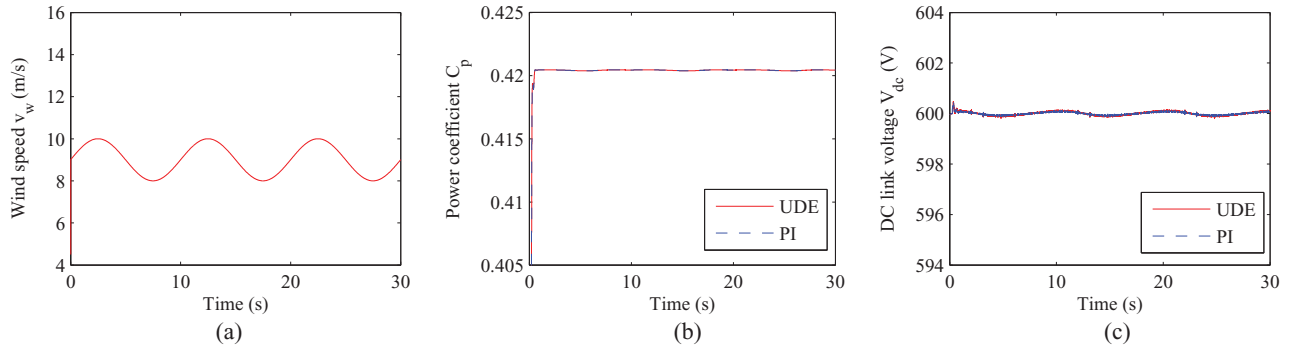


Figure 10. Nominal performance. (a) Wind speed v_w . (b) Power coefficient C_p . (c) DC-link voltage V_{dc} .

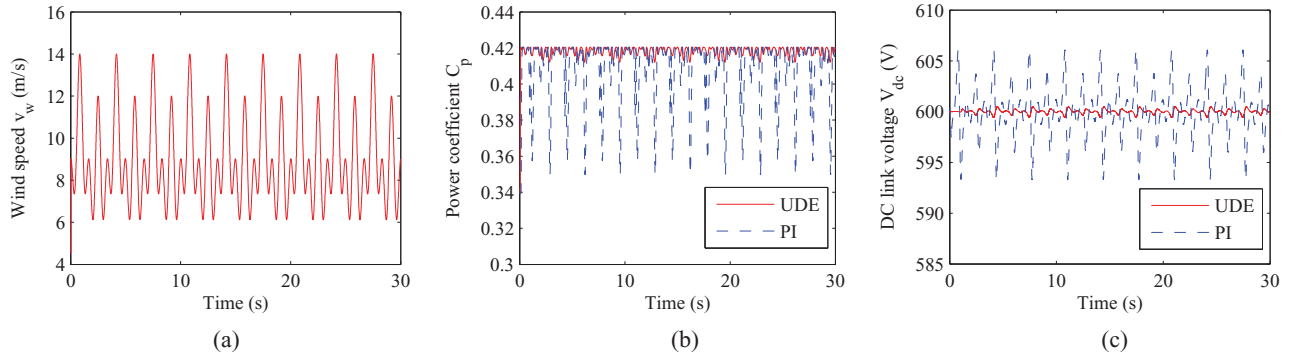


Figure 11. Robust performance. (a) Wind speed v_w . (b) Power coefficient C_p . (c) DC-link voltage V_{dc} .

to that of the UDE-based control when the wind speed is $v_w = [9 + \sin(0.2\pi t)]$ (m/s) (Case I). The simulation results are shown in Figure 10. For both control algorithms, the C_p is kept to be around the optimal value to capture the maximum wind power and the V_{dc} is kept more or less constant. The average real power generated with the UDE-based control is almost the same as that with the PI controller, as shown in Table 5.

To test the robustness of the proposed UDE-based control approach with comparison to the PI controller, another wind speed profile with different magnitudes and frequencies $v_w = [9 + \sin(0.6\pi t) + 2*\sin(1.2\pi t - \pi/2) + 2*\sin(2.4\pi t + \pi/2)]$ is considered as Case II. The simulation results are shown in Figure 11. Both the fluctuations of C_p and V_{dc} with the UDE-based control approach are smaller than those of the PI controller. The proposed UDE-based control approach can achieve better control performance than the PI controller for maintaining C_p to the optimal value and keeping V_{dc} stable. So, the proposed UDE-based control approach has better robustness to deal with both magnitude and frequency changes of wind speed than the PI controller. Also, the UDE-based vector control can achieve better current decoupling control with fast response for both the RSC with PMSG control and the GSC with power output control than PI controller. The UDE-based DC-link voltage regulation

control can regulate more stable DC-link voltage than the PI controller with model uncertainty and external disturbances under extreme varying wind speed conditions. The real power generated in both cases with the two different controllers is given in Table 5. The UDE-based control generates almost 5% more real power than the PI controller in this case.

7. Conclusion

In this paper, the UDE-based control approach has been applied for a PMSG-based variable-speed wind turbine system with back-to-back converters. The convective vector control has been modified with the UDE algorithm in both the rotor-side controller for the PMSG control and the grid-side controller for power output control to achieve the reliable current decoupling control with fast response. For maximum wind power capture, the optimal torque MPPT has been adopted in the rotor-side controller. For the DC-link voltage regulation, the UDE-based control has been developed to replace the conventional PI controller to deal with the model uncertainty and external disturbances in the grid-side controller. Simulation results of the whole system have been provided to demonstrate the good performance of the proposed UDE-based control approach in the presence of the

coupled dynamics, model uncertainty and external disturbances. Also, the proposed approach has shown better robustness to handle extreme varying wind conditions than the PI controller with higher real power generation.

Acknowledgements

The authors would like to thank the reviewers and the editors for their constructive and detailed comments and suggestions, which have helped significantly improve the quality of the paper.

Disclosure statement

No potential conflict of interest was reported by the authors.

References

- Bhowmik, S., Spee, R., & Enslin, J.H.R. (1999). Performance optimization for doubly fed wind power generation systems. *IEEE Transactions on Industry Applications*, 35(4), 949–958.
- Chedid, R., Karaki, S., & El-Chamali, C. (2000). Adaptive fuzzy control for wind-diesel weak power systems. *IEEE Transactions on Energy Conversion*, 15(1), 71–78.
- Chen, J., Ren, B., & Zhong, Q.-C. (2015, July). Hysteresis compensation in piezoelectric actuator positioning control based on the uncertainty and disturbance estimator. In *Proceedings of American Control Conference* (pp. 2537–2542), Chicago, IL.
- Chen, W.-H., Yang, J., Guo, L., & Li, S. (2015). Disturbance observer-based control and related methods: An overview. *IEEE Transactions on Industrial Electronics*. doi:10.1109/TIE.2015.2478397
- Fitzgerald, A.E., Kingsley, C., & Umans, S.D. (2003). *Electric machinery* (6th ed.). New York, NY: McGraw-Hill.
- Haque, M.E., Saw, Y.C., & Chowdhury, M.M. (2014). Advanced control scheme for an IPM synchronous generator-based gearless variable speed wind turbine. *IEEE Transactions on Sustainable Energy*, 5(2), 354–362.
- Heier, S., & Waddington, R. (1998). *Grid integration of wind energy conversion systems*. Chichester: Wiley.
- Johnson, K., Fingersh, L., Balas, M., & Pao, L. (2004). Methods for increasing region 2 power capture on a variable speed wind turbine. *Journal of Solar Energy Engineering*, 126(4), 1092–1100.
- Johnson, K., Pao, L., Balas, M., & Fingersh, L. (2006). Control of variable-speed wind turbines: Standard and adaptive techniques for maximizing energy capture. *IEEE Control Systems Magazine*, 26(3), 70–81.
- Kolhe, J.P., Shaheed, M., Chandar, T.S., & Taloe, S.E. (2013). Robust control of robot manipulators based on uncertainty and disturbance estimation. *International Journal of Robust and Nonlinear Control*, 23, 104–122.
- Leith, D.J., & Leithead, W.E. (1997). Implementation of wind turbine controllers. *International Journal of Control*, 66(3), 349–380.
- Li, S., Haskew, T.A., Swatloski, R.P., & Gathings, W. (2012). Optimal and direct-current vector control of direct-driven PMSG wind turbines. *IEEE Transactions on Power Electronics*, 27(5), 2325–2337.
- Li, S., Yang, J., Chen, W.-H., & Chen, X. (2014). *Disturbance observer-based control: Methods and applications*. Boca Raton, FL: CRC Press.
- Mohamed, Y.A.-R.I., & Lee, T.K. (2006). Adaptive self-tuning MTPA vector controller for IPMSM drive system. *IEEE Transactions on Energy Conversion*, 21(3), 636–644.
- Morimoto, S., Nakayama, H., Sanada, M., & Takeda, Y. (2005). Sensorless output maximization control for variable-speed wind generation system using IPMSG. *IEEE Transactions on Industry Applications*, 41(1), 60–67.
- Morimoto, S., Sanada, M., & Takeda, Y. (1994). Effects and compensation of magnetic saturation in flux-weakening controlled permanent magnet synchronous motor drives. *IEEE Transactions on Industry Applications*, 30(6), 1632–1637.
- Ozbay, U., Zergeroglu, E., & Sivrioglu, S. (2008). Adaptive backstepping control of variable speed wind turbines. *International Journal of Control*, 81(6), 910–919.
- Palejiya, D., Shaltout, M., Yan, Z., & Chen, D. (2015). Stability of wind turbine switching control. *International Journal of Control*, 88(1), 193–203.
- Rebeiro, R.S., & Uddin, M.N. (2012). Performance analysis of an FLC-based online adaptation of both hysteresis and PI controllers for IPMSM drive. *IEEE Transactions on Industry Applications*, 48(1), 12–19.
- Ren, B., & Zhong, Q.-C. (Nov. 2013). UDE-based robust control of variable-speed wind turbines. In *Proceedings of 39th Annual Conference of the IEEE Industrial Electronics Society* (pp. 3818–3823), Vienna.
- Ren, B., Zhong, Q.-C., & Chen, J. (2015). Robust control for a class of non-affine nonlinear systems based on the uncertainty and disturbance estimator. *IEEE Transactions on Industrial Electronics*, 62(9), 5881–5888.
- Sanz, R., Garcia, P., Zhong, Q.-C., & Albertos, P. (2015, June). Control of disturbed systems with measurement delays: Application to quadrotor vehicles. In *Proceedings of Control and Automation* (pp. 927–932), Torremolinos.
- Seixas, M., Melicio, R., & Mendes, V.M.F. (2014). Fifth harmonic and sag impact on PMSG wind turbines with a balancing new strategy for capacitor voltages. *Energy Conversion and Management*, 79, 721–730.
- Shariatpanah, H., Fadaeinedjad, R., & Rashidinejad, M. (2013). A new model for PMSG-based wind turbine with yaw control. *IEEE Transactions on Energy Conversion*, 28(4), 929–937.
- Simoes, M.G., Bose, B.K., & Spiegel, R.J. (1997). Design and performance evaluation of a fuzzy-logic-based variable-speed wind generation system. *IEEE Transactions on Industry Applications*, 33(4), 956–965.
- Sneyers, B., Novotny, D.W., & Lipo, T.A. (1985). Field weakening in buried permanent magnet AC motor drives. *IEEE Transactions on Industry Applications*, 21(2), 398–407.
- Soltani, M.N., Knudsen, T., Svenstrup, M., Wisniewski, R., Brath, P., Ortega, R., & Johnson, K. (2013, July). Estimation of rotor effective wind speed: A comparison. *IEEE Transactions on Control Systems Technology*, 21(4), 1155–1167.
- Song, Y.D., Dhinakaran, B., & Bao, X.Y. (2000). Variable speed control of wind turbines using nonlinear and adaptive algorithms. *Journal of Wind Engineering and Industrial Aerodynamics*, 85, 293–308.

- Sul, S.K. (2011). *Control of electric machine drive systems*. Hoboken, NJ: Wiley-IEEE Press.
- Sun, L., Zhang, Y., Li, D., Lee, K.Y., & Zhang, X. (2015, July). UDE-based 2-DOF control design for input/output delay system. In *Proceedings of American Control Conference* (pp. 3974–3979), Chicago, IL.
- Talole, S.E., Chandar, T.S., & Kolhe, J.P. (2011). Design and experimental validation of UDE based controller-observer structure for robust input–output linearisation. *International Journal of Control*, 84(5), 969–984.
- Talole, S.E., & Phadke, S.B. (2009). Robust input–output linearisation using uncertainty and disturbance estimation. *International Journal of Control*, 82(10), 1794–1803.
- Wu, B., Lang, Y., Zargari, N., & Kouros, S. (2011). *Power conversion and control of wind energy systems*. Hoboken, NJ: Wiley-IEEE Press.
- Yuan, X., Wang, F., Boroyevich, D., Li, Y., & Burgos, R. (2009). DC-link voltage control of a full power converter for wind generator operating in weak-grid systems. *IEEE Transactions on Power Electronics*, 24(9), 2178–2192.
- Zhang, Z., Zhao, Y., Qiao, W., & Qu, L. (2014). A space-vector-modulated sensorless direct-torque control for direct-drive PMSG wind turbines. *IEEE Transactions on Industry Applications*, 50(4), 2331–2341.
- Zhong, L., Rahman, M.F., Hu, W.Y., & Lim, K.W. (1997). Analysis of direct torque control in permanent magnet synchronous motor drives. *IEEE Transactions on Power Electronics*, 12(3), 528–536.
- Zhong, Q.-C., & Hornik, T. (2012). *Control of power inverters in renewable energy and smart grid integration*. Chichester: Wiley-IEEE Press.
- Zhong, Q.-C., Ma, Z., Ming, W.-L., & Konstantopoulos, G.C. (2015). Grid-friendly wind power systems based on the synchronverter technology. *Energy Conversion and Management*, 89, 719–726.
- Zhong, Q.-C., & Rees, D. (2004). Control of uncertain LTI systems based on an uncertainty and disturbance estimator. *Journal of Dynamic System, Measurement, and Control*, ASME, 126(4), 905–910.
- Zhu, B., Liu, H.H.-T., & Li, Z. (2015). Robust distributed attitude synchronization of multiple three-DOF experimental helicopters. *Control Engineering Practice*, 36, 87–99.